Magnetic nanoradiotracers for targeted neutrophil detection in pulmonary arterial hypertension

Lucía Fadón-Padilla[1,2], Claudia Miranda-Pérez de Alejo[2,3], Ana Beatriz Miguel-Coello[2], Marta Beraza[2], Desiré Di Silvio[2], Ainhize Urkola-Arsuaga[2], María Jesús Sánchez-Guisado[2], Irati Aiestaran-Zelaia[2,3], Laura Fernández-Méndez[2,3], Lydia Martinez-Parra[2], Ermal Ismalaj[2,4], Edurne Berra[5,6,7], Susana Carregal-Romero[2,4,7*] and Jesús Ruíz-Cabello[2,4,7,8*]

Abstract

Background Pulmonary arterial hypertension (PAH) is a severe disease characterized by elevated blood pressure in the pulmonary artery that can ultimately damage the right ventricle of the heart. PAH is pathophysiologically heterogeneous, which makes early diagnosis and treatment difficult. Inflammation is thought to be an important factor in the development and progression of this disease and may explain some of the observed interindividual differences. In the context of both acute and chronic inflammation, neutrophil recruitment to the lung has been suggested as a potential biomarker for studying PAH progression. However, there are currently no specific probes for its non-invasive in vivo detection. The imaging-based gold standard for assessing inflammation is $[^{18}F]$ fluorodeoxyglucose (^{18}F-FDG), which is not cell specific. This highlights the urgent need for more specific molecular probes to support personalized medicine.

Methods This study investigated the potential of magnetic nanoradiotracers based on ultrasmall iron oxide nanoparticles, functionalized with N-cinnamoyl-F-(D)L-F-(D)L-F peptide, to detect increased neutrophil infiltration in vivo in different PAH animal models via positron emission tomography. These nanoprobes target formyl peptide receptor 1, which is abundantly expressed in the cell membrane of neutrophils. To assess the benefit of these nanoprobes, their biodistribution was first assessed via magnetic resonance imaging and histology. Then, their lung uptake was compared by positron emission tomography with that of ^{18}F-FDG in two types of PAH animal models with different profiles of inflammation and neutrophil infiltration: monocrotaline and double-hit Sugen-chronic hypoxia PAH rat models.

Results Our targeted magnetic nanoradiotracer detected an increase in pulmonary neutrophil infiltration in both PAH models and distinguished between them, which was not possible with ^{18}F-FDG PET.

Conclusions This study underscores the importance of targeted imaging in providing an individualized and longitudinal evaluation of heterogeneous and multifactorial diseases such as PAH. The use of targeted multimodal

*Correspondence:
Susana Carregal-Romero
scarregal@cicbiomagune.es
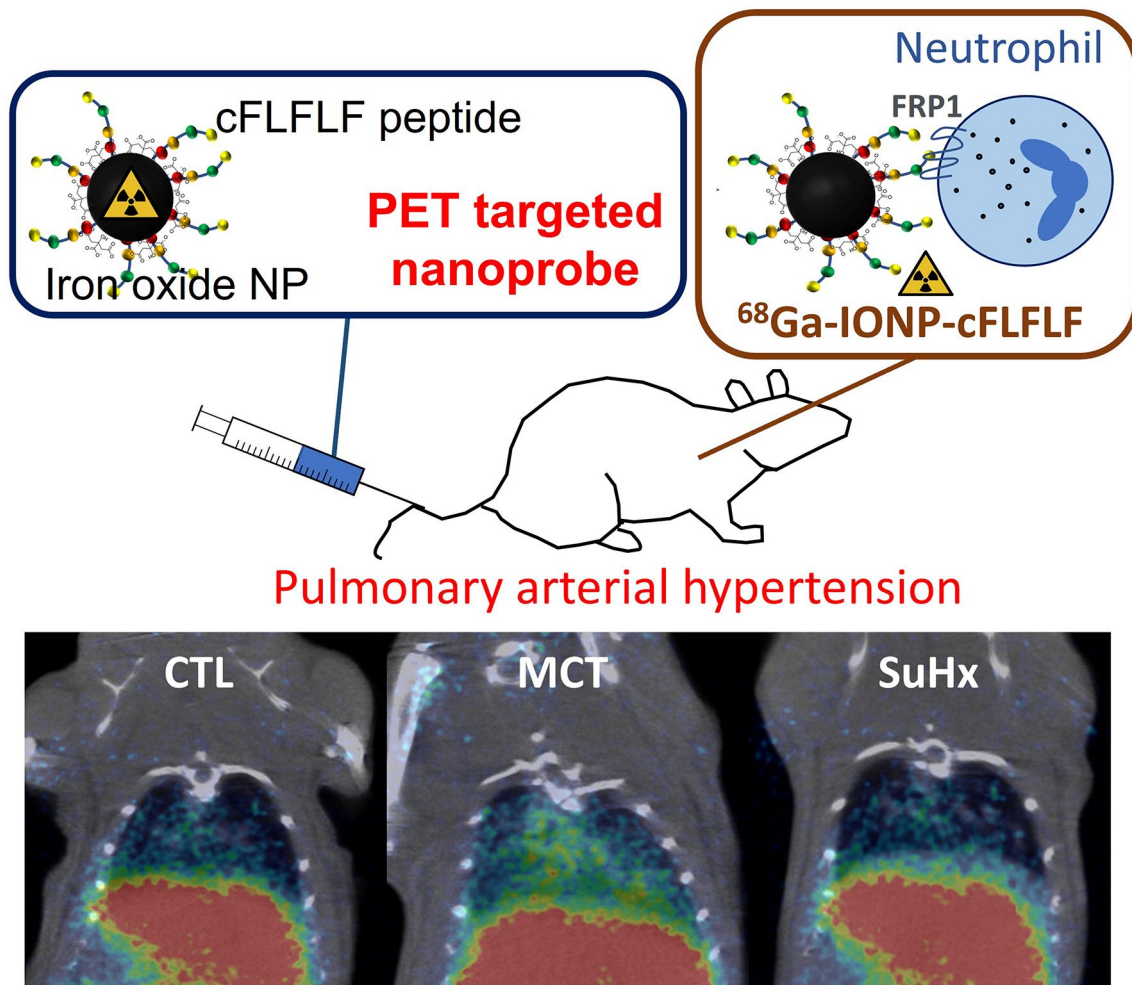Jesús Ruíz-Cabello
jruizcabello@cicbiomagune.es
Full list of author information is available at the end of the article

nanoprobes, for magnetic resonance/positron emission tomography imaging has the potential to facilitate the diagnosis and monitoring of diseases, as well as the development of novel therapies.

Graphical abstract

Introduction

Pulmonary arterial hypertension (PAH) is a complex and life-threatening disease involving inflammatory processes in the lungs of all patients. However, the exact timing and extent of inflammation remain unknown [1, 2]. Neutrophils, key effector cells of the innate immune system, have recently been implicated in pathological angiogenesis, vascular dysfunction, and disease severity [3, 4]. Therefore, neutrophils are key biomarkers for improving our understanding of PAH and are potential novel diagnostic tools. Attempts to characterize their infiltration in PAH have been unsuccessful due to the heterogeneity of the disease among patients and the lack of tools to monitor specific cell populations using non-invasive techniques. To overcome this obstacle, in vivo imaging of neutrophils may help to characterize the pathology and facilitate the diagnosis and treatment of PAH.

^{18}F-fluorodeoxyglucose (^{18}F-FDG) positron emission tomography (PET) imaging is widely used to monitor inflammatory processes in PAH and other diseases in vivo [5–7], but its limitation lies in the lack of cellular specificity, necessitating the development of novel imaging tools. In a seminal study by Jun-Bean Park et al., targeted ligand-mediated imaging was shown to specifically detect macrophage infiltration in the lungs of a monocrotaline (MCT) rat model of PAH [8]. They used

the ^{68}Ga-2-(p-isothiocyanatobenzyl)-1,4,7-triazacy-clononane-1,4,7-triacetic acid (NOTA) mannosylated human serum albumin (MSA) radiotracer, which specifically binds to the mannose receptor of macrophages. This allowed their quantification in the lung. This approach holds promise for more precise and specific imaging of inflammatory processes in PAH and other diseases and may be useful for the early diagnosis of this pathology.

Inspired by this work, we investigated the feasibility of using a similar strategy for ligand-mediated imaging of neutrophils, but with nanoparticles (NPs) in the 10–50 nm diameter range, which tend to circulate in the bloodstream for longer periods than small molecules [9], potentially increasing their targeted accumulation in the lung. This is due to several key factors, including size-dependent clearance mechanisms. One of them is renal filtration. Small molecules are rapidly cleared by the kidneys, which efficiently filter particles smaller than 5–10 nm. In contrast, NPs in the 10–50 nm range are large enough to avoid immediate renal clearance, allowing them to remain in the circulation longer. The reticuloendothelial system (RES) can also be evaded by NPs smaller than 50 nm. Larger particles (>100 nm) are easily recognized and cleared by macrophages in the liver and spleen. Finally, smaller nanoparticles are less affected by margination (movement towards vessel walls) in blood flow compared to larger particles, which helps them stay in the central circulation longer. In conclusion, a size range of 10–50 nm is convenient for enhancing circulation times, as it is large enough to avoid rapid renal clearance but small enough to evade immediate RES uptake. This allows NPs to achieve significantly longer circulation times than those of small molecules after intravenous administration.

Our ligand of choice was the cycled peptide N-cinnam-oyl-F-(D)L-F-(D)L-F (cFLFLF), an antagonist of formyl peptide receptor 1 (FPR1) [10], which is highly expressed on the plasma membrane of neutrophils in response to inflammatory stimuli [11]. FLFLF has high neutrophil binding affinity and has been successfully used to characterize neutrophil infiltration in several preclinical models, including tuberculosis, acute osteomyelitis and pulmonary ischemia-reperfusion injury [12–14]. These previous in vivo studies were based on more fundamental in vitro studies using FPR1-expressing cells and neutrophils isolated from patients to determine the binding affinity of the peptide to this membrane receptor [14, 15].

Recently, we demonstrated that this hydrophobic peptide can be covalently bound to citrate-coated ultrasmall (∼ 10 nm) iron oxide nanoparticles (IONPs) via carbodiimide chemistry when the peptide contains a terminal lysine residue [16]. We used a fast hydrothermal microwave-assisted method to prepare IONPs, which allowed radiolabeling of the IONP core with ^{68}Ga to produce multimodal probes for both magnetic resonance imaging (MRI) and PET. We demonstrated by PET imaging that ^{68}Ga-IONP-cFLFLF is useful for detecting acute inflammatory processes in the lung in a mouse model of lipopolysaccharide-induced inflammation [17].

In this study, we synthesized similar target-specific iron-oxide based nanoprobes to compare neutrophil infiltration in different PAH animal models in vivo. Using PET imaging, we found significant differences in neutrophil lung infiltration between monocrotaline (MCT) and double-hit Sugen-chronic hypoxia (SuHx) PAH rat models. These findings were confirmed by histological analysis. In addition, biodistribution analysis in healthy rats using MRI data and histology revealed negligible accumulation of these nanoprobes in the lungs. Finally, we compared the performance of ^{68}Ga-IONP-cFLFLF with that of ^{18}F-FDG for the PET imaging of neutrophil infiltration. No differences in lung ^{18}F-FDG uptake were observed, indicating the superiority of ^{68}Ga-IONP-cFLFLF in neutrophil infiltration studies in PAH animal models.

Methods

Synthesis of ^{68}Ga-IONP-cFLFLF

We first prepared citric acid-coated ^{68}Ga-IONPs according to the synthetic procedure of Pellico et al. [18]. Briefly, the ^{68}GaCl$_3$ (aq) precursor was eluted from the ^{68}Ge/^{68}Ga generator with 1 mL 0.05 M HCl at a rate of 1 mL/min and added directly to a microwave tube containing 18.7 mg of FeCl$_3$·6H$_2$O (0.07 mmol) and sodium citrate dihydrate (20 mg, 0.068 mmol) dissolved in 1.25 mL of Milli-Q water. The activity of this mixture was 4.59 mCi. Then, 0.25 mL of NH$_2$NH$_2$H$_2$O was added, and the microwave (Monowave 300, Anton Paar Germany GmbH73760 Ostfildern-Scharnhausen Germany, equipped with an internal temperature probe and external IR probe) was ramped up to 100℃ for 1 min, and then held at 100℃ for 10 min. The mixture was cooled to 60℃ and the sample was purified using a PD-10 desalting column packed with Sephadex-25 resin (previously activated with 25 mL of ultrapure Milli-Q water). The sample solution was collected in a vial, yielding 2.5 mL of ^{68}Ga-IONP solution, the concentration of which was measured by inductively coupled plasma-mass spectrometry (ICP-MS) as [Fe]=1.28 mg/mL. Surface functionalization of the nano-radiotracer was achieved by mixing 2.5 mL of ^{68}Ga-IONP-citrate (2.75 mCi) with 13.4 mg of N-(3-dimethylaminopropyl)-N'-ethylcarbodiimide hydrochloride (EDC) and 16.3 mg and N-hydroxysulfosuccinimide (sulfo-NHS) and stirring the mixture for 30 min. Purification was performed by centrifugation (10.35 × g, 4 min) through six AMICON 30 K filters (cut-off 30 kDa). The retentate was resuspended in 1.5 mL of PBS (0.01 M, pH 8), and 0.8 mg of peptide cFLFLF(K)

with a terminal lysine residue (dissolved in 50 μL DMSO) was added to the solution and stirred for 1 h. The sample was subsequently centrifuged again (10.35 x g, 4 min) using two AMICON 30 K filters. The sample was diluted in 400 μL of saline (0.9%) for each filter (800 μL total, 412 μCi). To prepare the final injectable doses, the appropriate amount of nanoparticle solution with the desired activity was taken with a syringe before proceeding to administration. The total synthesis time from elution was approximately 140 min. ICP-MS: [Fe]=1.81 mg/mL in the final solution.

Physicochemical characterization of ^{68}Ga-IONP-cFLFLF

Decayed IONP-cFLFLF was used for physicochemical characterization. Transmission electron microscopy (TEM) characterization was performed with a LaB6-TEM (JEOL JEM-1400PLUS (40 kV −120 kV) instrument equipped with a GATAN US1000 CCD camera (2k × 2k). Ion-coupled mass spectrometry (ICP-MS) was used to determine the Fe content of each sample. Both, the hydrodynamic diameter and the zeta potential of the NPs of the NPs were measured using a Malvern Zetasizer Nano-ZS (Malvern Instruments, Malvern, UK). X-ray photoelectron spectroscopy (XPS) experiments were performed in a SPECS Sage HR 100 spectrometer with a non-monochromatic X-ray source (aluminum Kα line of 1486.7 eV energy and 252 W), which was placed perpendicular to the analyzer axis and calibrated using the 3d5/2 line of Ag with a full width at half maximum (FWHM) of 1.1 eV. FT-IR) spectra were measured using a Bruker Invenio-X FT-IR spectrophotometer, controlled using OPUS 9 software.

Magnetic relaxometry measurements

The spin-lattice and spin–spin relaxation times (T_1 and T_2) were measured for five concentrations of both the IONP and IONP-cFLFLF samples to obtain r_1 and r_2 in a Bruker Minispec MQ60 (Bruker Biospin GmbH) contrast agent analyzer at 1.5 T and 37 °C. T_1 and T_2 were also measured using a 7 T horizontal bore Bruker Biospec USR 70/30 MRI system (Bruker Biospin GmbH).

Animal models of PAH and phenotypic evaluation

The biodistribution study was conducted on a group of $n=4$ eight-weeks old Sprague-Dawley female rats (Janvier Labs) administered with 1.49 mg/kg of Fe determined by ICP-MS. In vivo MRI studies were carried out on a 7 T Bruker Biospec USR 70/30 MRI system (Bruker Biospin GmbH, Ettlingen, Germany), interfaced with an AVANCE III console and a BGA 12-S imaging gradient insert (more information can be found in the Supporting Information). PH experiments were performed with six to eight-weeks-old RjHan: Sprague-Dawley female rats (Janvier Labs) divided into three groups ($n=8$/each group): the normoxia control (CTL), MCT and SuHx groups. For the MCT-induced model, the rats received a single intraperitoneal injection of 60 mg/kg MCT (C2401, Sigma-Aldrich), which was dissolved in 1 M HCl and neutralized with NaOH. We limited the study to three weeks after injection.

In the SuHx model, rats were injected subcutaneously at the beginning of the experiment with 20 mg/kg vascular endothelial growth factor (VEGF) inhibitor (Sugen 5416 or Sugen; Tocris) dissolved in vehicle (polysorbate 80 0.4% [v/v], methyl cellulose 0.5% [w/v], and benzyl alcohol 0.9% [v/v] in saline solution) and exposed to normobaric hypoxia at 10% O_2 inside a hypoxic workstation (BioSpherix) for three weeks, followed by a week under normoxia (20% O_2). The CTL group received a subcutaneous injection of vehicle and remained normoxic throughout the experiment. After PH induction, four animals from each group were characterized by cardiac MRI without contrast agents. ^{18}F-FDG PET imaging was performed prior to perfusion with heparinized saline for lung and heart harvesting, generation of paraffin blocks, and histological examination. The remaining rats ($n=4$) were subjected to neutrophil-targeted imaging via ^{68}Ga-IONP-cFLFLF PET and RVSP measurements. More information about the preclinical evaluation of the PH model can be found in the Supporting Information.

Positron emission tomography and computed tomography (PET/CT) imaging

PET and micro-CT imaging acquisitions were sequentially performed using the β (PET) and X-cube (CT) microsystems of Molecubes® (MOLECUBES NV), respectively. The rats were injected with the corresponding radiotracers. In each case, ^{18}F-FDG (100–180 μCi) or ^{68}Ga-IONP-cFLFLF (65–150 μCi) were intravenously injected through the tail vein and imaged 30 min post-administration when both tracers were no longer in circulation by static 10 min scan whole-body images (1 bed). Anesthesia was induced by 4–5% isoflurane inhalation in pure O_2 and maintained at a 1.5-2% flow rate based on respiration-rate monitoring (60–80 bpm), and the animals were maintained warm throughout the imaging experiment. One-bed imaging acquisition was performed using a 511 keV±30% energetic window. CT acquisitions were generally performed at the end of each PET scan for anatomic information and attenuation correction, providing unambiguous localization of the radioactive signal. Reconstruction of the images was performed using the mathematical algorithm 3D-OSEM (3D ordered subset expectation maximization; 30 iterations). For each animal, PET-CT images were co-registered and analyzed using PMOD image analysis software (PMOD Technologies Ltd., Zürich, Switzerland). The volumes of interest (VOIs) were manually outlined on the organs of interest

in the CT images. VOIs were transferred to PET images, and activity values normalized to the initial amount of radioactivity were obtained as the mean standard uptake values (SUV_{mean}).

Histological analysis

Lung and heart tissues were fixed with 10% formaldehyde for 24 h at room temperature (RT), dehydrated with alcoholic solutions, and embedded in paraffin. Lung tissues were then cut into 5-μm sections and stained with an elastic stain kit (HT25A-1KT, Sigma-Aldrich). The slides were digitalized using a Cell Axio Observer microscope (ZEN). Images (20x) were taken on a tile covering the entire lung and stitched together to identify the pulmonary arteries throughout the tissue. Five peripheral vessels adjacent to the airways in the transverse orientation (the longest side did not exceed twice the length of the shortest side) were randomly selected from all the lung tissues. The medial wall thickness, lumen diameter, and medial wall cross-sectional area of the small arteries (40–80 μm outer diameter) were determined via the open-source software ImageJ (version 1.53). The diameter of the lumen was delimited to the point of greatest length on all occasions. These measurements have facilitated the use of two indices to quantify the type and degree of vascular remodeling: percent medial wall thickness (medial wall thickness/inner diameter × 100) and percent medial wall area (medial wall cross-sectional area/total cross-sectional area × 100).

Immunohistochemical (IHC) analysis

Five-micron-thick paraffin-embedded lung tissue sections were deparaffinized with xylene and ethanol at decreasing concentrations. Antigen retrieval was performed using sodium citrate buffer (pH 6) in a vegetable steamer over a 45-min cycle, after which the mixture was allowed to cool for 2 h at RT. The next step was involved incubation with a drop of endogenous blocking solution for 10 min at RT to prevent hydrogen peroxidase inhibition. After being washed with 0.1% Triton-PBS, the tissues were incubated with a blocking solution (bovine serum albumin 1% + goat serum 2% + PBS+Triton 0.1%) for 30 min at RT in a humid chamber. The slides were subsequently incubated with an anti-myeloperoxidase antibody (ab9535, Abcam) overnight at 4 °C in a humid chamber. The following day, after washing thoroughly with 0.1% Trinton-PBS, the slides were incubated with the secondary antibody for 30 min at RT in a humid chamber. Signal amplification was then performed for 30 min. Peroxidase activity was developed via DAB working solution, and the samples were observed under a microscope. The reaction was stopped by rinsing the slides with deionized water before hematoxylin counterstaining. For Prussian blue staining, paraffin-embedded

Sect. (4 μm) of the lungs mounted on glass slides were deparaffinized with xylene and ethanol at decreasing concentrations and then washed with distilled water. The slides were then stained for 1 h at 60 °C with Perls solution obtained by mixing the same quantity of 7% potassium ferrocyanate trihydrate in Milli-Q water and 7% HCl. After being washed in water, the samples were stained with 0.1% nuclear fast red-aluminum sulphate solution (#1001210500, Sigma-Aldrich) for 2 min. Finally, the samples were washed with increasing concentrations of ethanol and xylene and mounted in synthetic mounting medium (DPX).

Statistical analysis

Statistical analysis was performed using the GraphPad 9.0.2 software. One-way analysis of variance (ANOVA) was used to correct for multiple comparisons, and the Šidák correction was used for statistical hypothesis testing. The values are presented as the mean±SD unless otherwise noted. The p-values are represented by asterisks as follows: * $p < 0.05$, ** $p < 0.01$, *** $p < 0.001$, and **** $p < 0.0001$. Differences were considered statistically significant at $P < 0.05$.

Results and discussion

Synthesis of cFLFLF-functionalized radiolabeled iron oxide nanoparticles

In recent years, the synthesis of hydrophilic metal oxides via microwave-assisted methods has facilitated the development of time-efficient synthetic protocols for different types of nanoparticles (NPs) [19–21]. This advancement enables the generation of iron oxide-based NPs with diverse chemical compositions and surface coatings, due to their straightforward core doping and tailorable surface chemistry composition [21, 22]. The core doping process involves a library of cationic metals and radioisotopes, such as Mg^{2+} or $^{68}Ga^{3+}$, and a mixture of them (e.g., Zn^{2+}/Ga^{3+}). This modulates the relaxometric properties of iron oxide NPs for MRI or provides the emission of positrons for PET. Moreover, subsequent chemical modification of the coating with ligands can facilitate targeted imaging of highly studied diseases such as atherosclerosis or cancer [23, 24]. However, some rare diseases such as PAH could also benefit from this technology, as demonstrated in this work.

In our study, we followed the protocol established by Pellico et al. [16] to synthesize ^{68}Ga-IONP and ^{68}Ga-IONP-cFLFLF (Fig. 1A) and evaluated the efficacy of the later efficacy in distinguishing between different neutrophil infiltration scores in two different PAH animal models. Both ^{68}Ga-IONP and ^{68}Ga-IONP-cFLFLF were decayed for a minimum of 24 h before characterization via transmission electron microscopy (TEM), dynamic light scattering (DLS), Fourier transform infrared (FTIR)
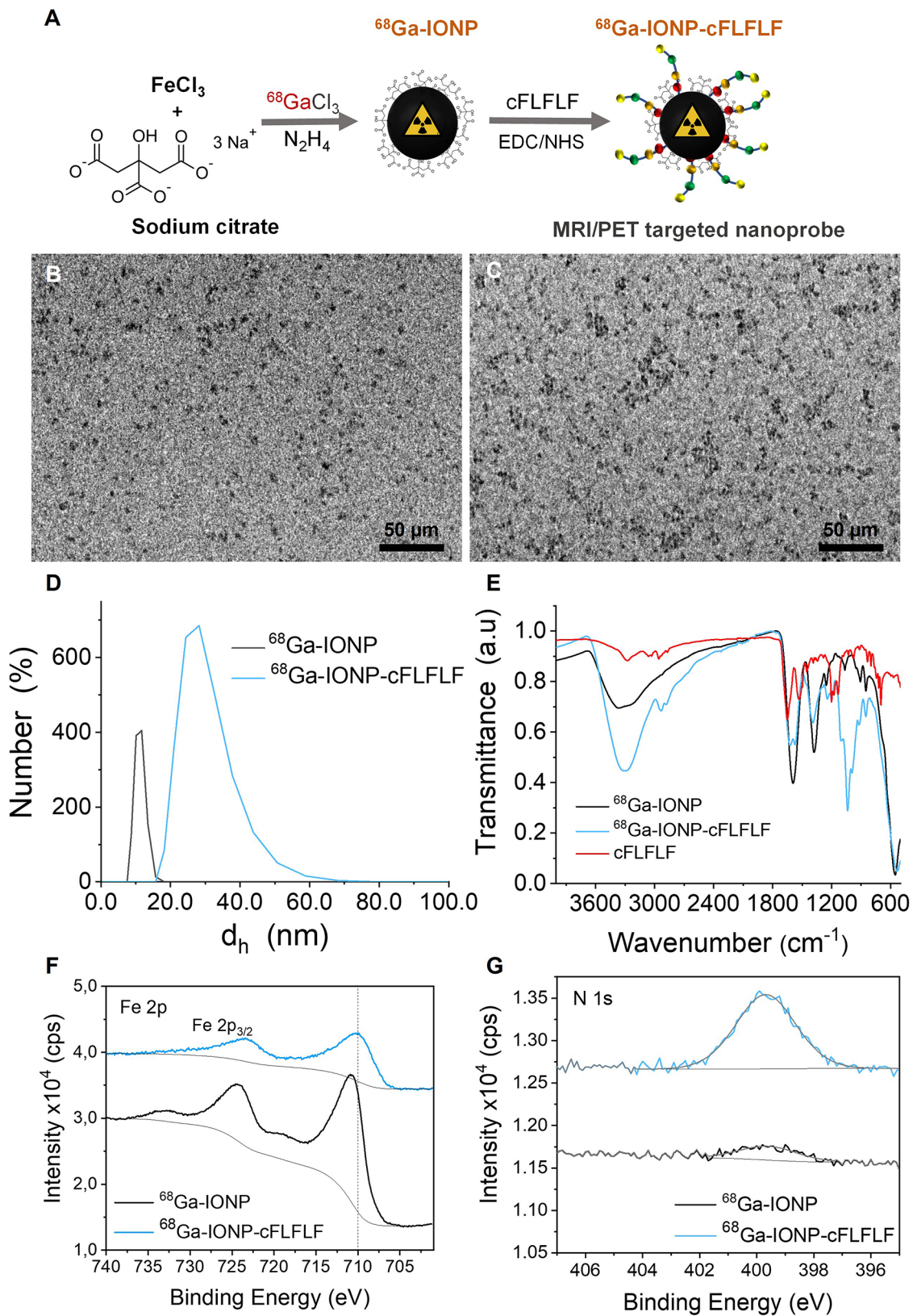
Fig. 1 **A**) Schematic representation of the synthesis of the ^{68}Ga-IONP-cFLFLF nanoradiotracer. **B**) TEM image of ^{68}Ga-IONPs. **C**) TEM image of ^{68}Ga-IONP-cFLFLF. **D**) Hydrodynamic diameter (d_h) of IONPs before and after functionalization with cFLFLF(K). **E**) FT-IR spectra of ^{68}Ga-IONP-cFLFLF, ^{68}Ga-IONP, and cFLFLF(K). **F**) XPS spectra of the core level of Fe 2p and N 1s (**G**) before and after cFLFLF(K) functionalization

spectroscopy, and X-ray photoelectron spectroscopy (XPS).

TEM characterization (Fig. 1B and C) revealed slight nanoparticle clustering following surface functionalization. This clustering was likely due to the hydrophobic nature of the cFLFLF peptide and attractive interactions between the nanoparticles during the drying process. DLS measurements demonstrated a moderate increase in the hydrodynamic diameter (d_h) of IONP after conjugation with cFLFLF(K). The d_h of ^{68}Ga-IONP and ^{68}Ga-IONP-cFLFLF were determined to be 11.4±1.4 and 39.1±10.5 nm, respectively. This confirms their minimal degree of clustering and a size range of 30–60 nm, which is optimal for driving the membrane wrapping process required in ligand-mediated targeting (Fig. 1D) [9]. This size augmentation correlated with a shift in zeta potential from −23.0±2.5 eV to -6.9±2.6 eV after surface modification, which is attributable to a reduction in citrate carboxylic groups on the IONP surface.

Furthermore, FTIR analysis of free cFLFLF(K), ^{68}Ga-IONP, and ^{68}Ga-IONP-cFLFLF confirmed the incorporation of cFLFLF(K) into the citrate-coated IONP (Fig. 1E). This was evidenced by the simultaneous appearance of characteristic bands of citrate at 1594 cm^{-1} and 1379 cm^{-1} (asymmetric and symmetric stretching modes of COO$^-$) [25, 26], and the bands associated with the cFLFLF(K) ligand at 2935 cm^{-1}, 1621 cm^{-1}, and 995 cm^{-1}, corresponding to aromatic C-H stretching and olefin groups, respectively [16, 27]. XPS further confirmed the incorporation of cFLFLF(K) on the NP surface (Fig. 1F-G). Table S1 lists the atomic percentages of the main elements of the nanoradiotracers, C, O, N, Fe, and Zn (from ^{68}Ga decay), showing a decrease in the relative amount of Fe and C, and an increase in the amount of O and N due to the cFLFLF(K) peptide coating. Figure 2F shows the XPS spectra of the Fe 2p peaks, which highlights a decrease in the intensity after peptide conjugation due to the thickening of the coating. Conversely, an increase in the N 1s intensity at 399.8 eV was observed
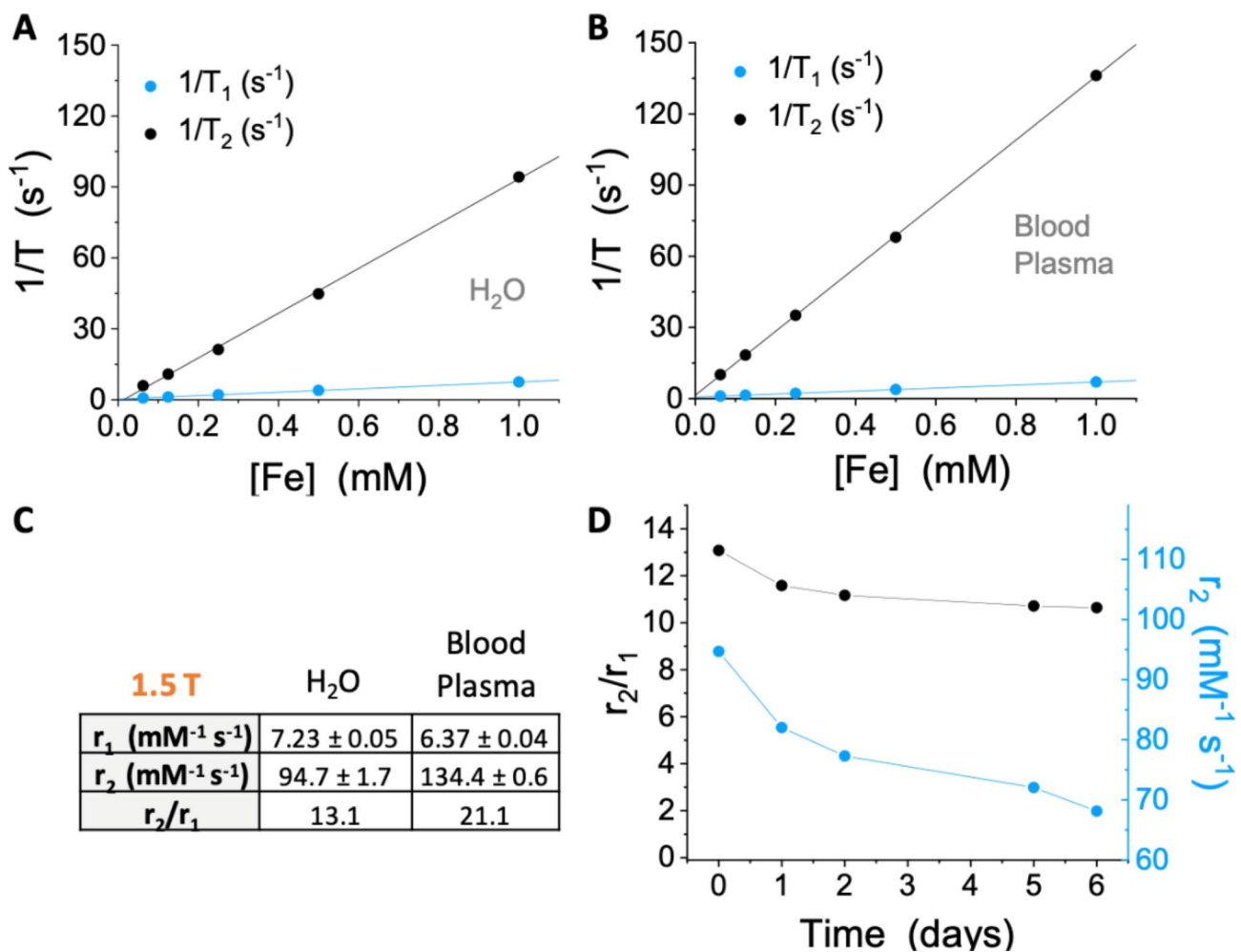

Fig. 2 T_1 and T_2 relaxation rates of IONP-cFLFLF in water (**A**) and blood plasma (**B**) at 1.5 T. **C**) Longitudinal and transverse relaxivities and their corresponding r_2/r_1 ratios at 1.5 T. **D**) Temporal stability of r_2/r_1 and r_2 in H_2O

(Fig. 2G), confirming the presence of the lysine conjugated peptide. In summary, the observed increase in the nanoradiotracer d_h, increase in zeta potential, and shift in chemical composition confirmed successful peptide conjugation, resulting in the formation of the ^{68}Ga-IONP-cFLFLF nanoradiotracer.

^{68}Ga-IONP-cFLFLF relaxometric properties

To assess the potential of ^{68}Ga-IONP-cFLFLF as an effective MRI/PET contrast agent, we conducted thorough relaxometric analyses using a 1.5 T relaxometer in both aqueous and blood plasma solutions with increasing concentrations of nonradioactive IONP-cFLFLF (see Fig. 2A and B). These NPs have physicochemical properties similar to those of their radiolabeled counterparts, as radioisotopes are found in trace amounts [18]. Our results revealed a consistent inverse relationship between iron concentration and longitudinal and transverse T_1 and T_2 relaxation times in both types of fluid (water and blood plasma), which is indicative of the MRI contrast-enhancing capabilities of the IONP-cFLFLF. The longitudinal and transverse relaxation rates (r_1 and r_2) shown in Fig. 2C underscore the exceptional performance of IONP-cFLFLF as a T_2 or negative MRI contrast agent. When we compared the relaxometric properties of IONP-cFLFLF with those of IONP before peptide functionalization ($r_1 = 7.6$ mM^{-1} s^{-1} and $r_2 = 18.3$ mM^{-1} s^{-1}, Figure S1), we observed a shift in the relaxation rates, indicating a low degree of clustering [28], as observed in DLS measurements (Fig. 1D). Blood plasma induced a slight decrease in r_1 and an increase in r_2, which maintained the MRI contrast in the negative contrast regime. The effect of the components of blood plasma on magnetic NPs depends on various factors, including the specific properties of the NPs, the composition of the blood plasma, and the interactions between the NPs and plasma components. Proteins in the blood plasma can create steric hindrance around magnetic NPs, reducing the mobility of water molecules near the NP surface. This reduced mobility can decrease the efficiency of water relaxation and thus affect both the longitudinal and transverse relaxivities. Our results indicate that the MRI contrast agent capabilities are not reduced in blood, but rather the opposite, but a systematic study will be needed to understand the intricate effect of the protein corona on the relaxometric properties of these types of magnetic NPs. Notably, our investigation of temporal contrast stability over one week (Fig. 2D) revealed a decrease in r_2/r_1 and r_2 while maintaining negative MRI contrast behavior, which is crucial for maintaining optimal contrast enhancement over time.

Biosafety and biodistribution

Before ^{68}Ga-IONP-cFLFLF was evaluated for biodistribution studies and targeted imaging, cell viability assays were conducted in the HepG2 human liver cell line (broadly used for hepatotoxicity studies) and lung carcinoma epithelial A549 cells (Figure S2). The results obtained with HepG2 and A549 cells indicated a negligible influence of the NPs on cell viability at iron concentrations as high as 150 and 75 μg/mL, respectively. Considering the dilution effect of NPs when administered in the blood and the Fe doses typically used for MRI (1.8–5.4 μg/kg) [29, 30], NPs appear to be safe in terms of cytotoxicity in both cell lines. However, to fully elucidate their biosafety profile, further studies are needed across a broader range of cell lines and at multiple time points. These studies should investigate their effects on for example cellular oxidative stress, potential genotoxicity, and their influence on glutathione-dependent antioxidant defenses [31].

In addition to these cellular assays, it is important to analyze blood plasma biomarker levels related to potential hepatic (alanine transaminase, aspartate transaminase, total bilirubin) and renal damage (blood urea nitrogen, phosphorus) [32]. Furthermore, to assess pulmonary safety, markers of lung inflammation should be measured. Biomarkers such as interleukin-6 (IL-6), tumor necrosis factor-alpha (TNF-α), interleukin-1 beta (IL-1β), and C-reactive protein (CRP) could provide insights into the inflammatory response in lung tissue. Elevated levels of these markers might indicate acute or chronic inflammation, which is critical to assess for potential pulmonary toxicity.

Regarding the NP biodistribution, to exclude nonspecific accumulation of ^{68}Ga-IONP-cFLFLF in the lungs, we studied the biodistribution of control NPs (IONP-cFLFLF without ^{68}Ga) in healthy animals after similar intravenous administration prior to performing targeted PET imaging assays in animal models of PAH. MRI allowed longer scan times than PET analysis (^{68}Ga $T_{1/2} = 68$ min) and evaluation of the clearance and accumulation of the NPs in different organs within 24 h. Figure 3A shows representative T_2 maps in the coronal view of the animals, where the contrast of the kidneys, spleen, and liver changed during the time course of the study due to the accumulation of NPs. Figure 3B-D provides the average data ($n = 3$) of the transverse relaxation time T_2 for the different organs where the NPs mainly accumulated. The recovery of the T_2 value in the kidneys shown in Fig. 3B can be explained by assuming partial renal elimination of these NPs 24 h post-administration. Although NPs have a mean size larger than the kidney threshold, due to the polydispersity of the NPs, it is possible that some of the smaller NPs undergo renal elimination, as has been observed previously with similar NPs [21]. In contrast, in
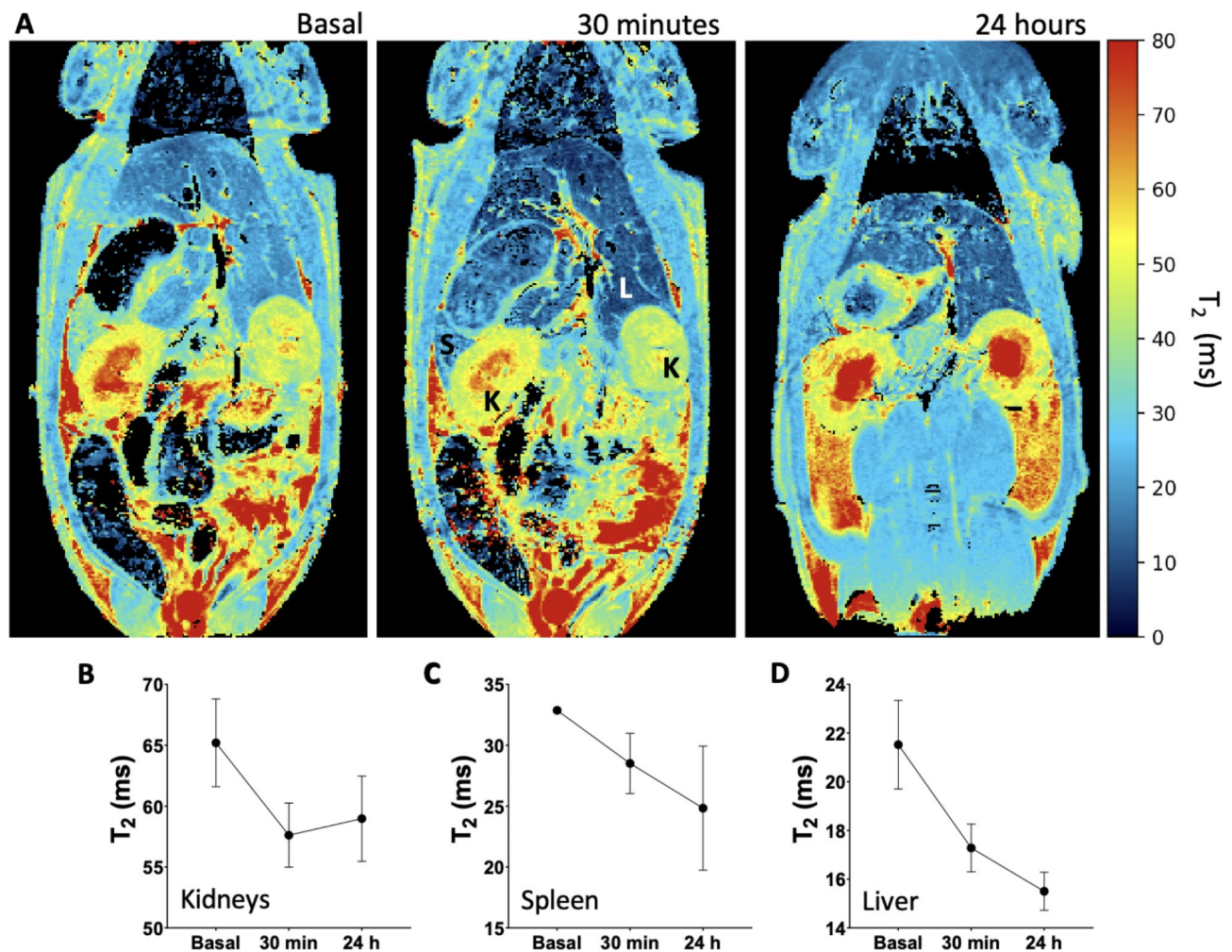
Fig. 3 **A**) Coronal views of T_2 relaxation maps of a rat i.v. injected with IONP-cFLFLF showing a reduction in this parameter and accumulation of nanoparticles in the liver (L), spleen (S), and kidneys (K). The T_2 values (*n* = 3) for the kidneys (**B**), spleen (**C**), and liver (**D**) were plotted at two different time points (30 min, 2 h) after basal measurements (before the i.v. administration of the nanoparticles)

the case of the liver and spleen, the results indicated that there was an initial accumulation of NPs at half an hour that increased with time (Fig. 3C, D).

The 24-hour accumulation of IONP-cFLFLF in different organs was investigated via Prussian blue staining, as shown in Fig. 4. Owing to the iron-rich nature of the spleen, even under basal conditions, it was not possible to visualize the presence of the NPs. However, images taken from the kidneys (Fig. 4A) revealed no detectable accumulation of NPs, whereas in the liver, their presence was evident from the characteristic blue staining observed in Kupffer cells located in hepatic sinusoids (Fig. 4B). Furthermore, histological samples of the lungs obtained 24 h after i.v. administration demonstrated that these NPs did not accumulate in this organ (Fig. 4C). Recently, published results from positron emission single-particle tracking have shown that larger uncoated silica NPs (≈1 µm) accumulate persistently in the lung after intravenous administration, which is likely associated with

intracapillary retention after protein corona formation [33]. Our results obtained with IONP-cFLFLF suggest negligible lung accumulation even after i.v. administration, which may also indicate the absence of extensive NP agglomeration in the blood, as shown by the relaxometric properties in Fig. 2D. Finally, we performed H&E staining of various organs involved in NP clearance (Figure S3). Histopathologic evaluation of these organs revealed negligible inflammation and tissue necrosis after IONP-cFLFLF administration.

Targeted imaging of neutrophil infiltration in pulmonary arterial hypertension

The aim of our study was to demonstrate that ^{68}Ga-IONP-cFLFLF is a suitable tool for comparing neutrophil infiltration profiles via noninvasive molecular imaging and to compare the results of two different preclinical models of PAH. While no animal model of PAH perfectly recapitulates human PAH, rodent and rat models of MCT
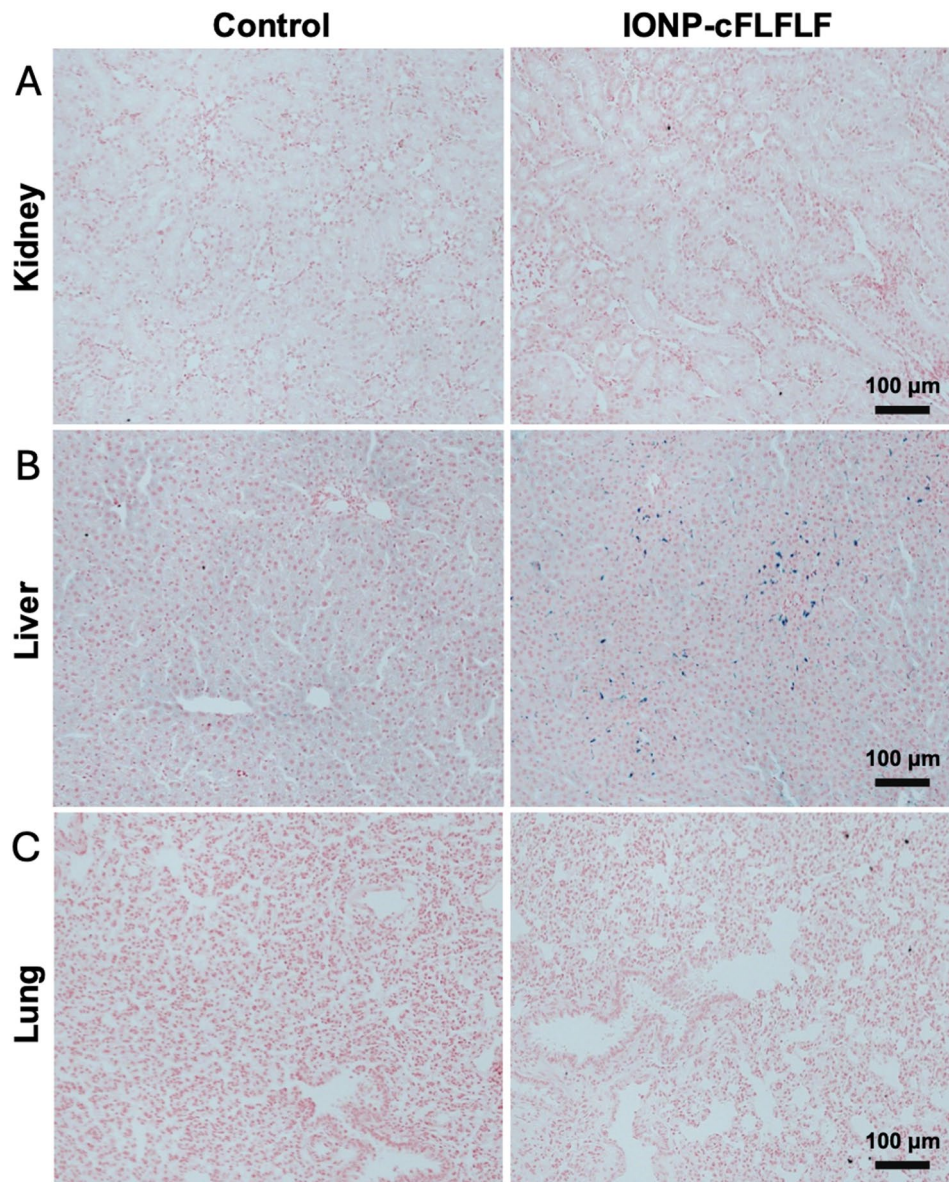
Fig. 4 Histological determination of the presence of IONP-cFLFLFs in different tissues was performed via Perl's Prussian blue staining of Fe^{3+} after 24 h of intravenous administration, and the results were compared with those of control tissues from non-treated animals in the **A**) kidney, **B**) liver, and **C**) lung

and SuHx are widely used to provide important insights into the pathogenesis and treatment of the disease [34, 35], although they have very different etiopathologies. We use of three weeks of exposure to hypoxia and monocrotaline-treated animals after three weeks of its administration to ensure progression of disease mechanisms in both models, allowing a meaningful comparison of the development and characteristics of PAH [36, 37]. Our study aimed to further characterize the inflammatory process in these two models using targeted PET imaging with a novel nanoradiotracer and to compare it with ^{18}F-FDG as a reference for such a process. The role of neutrophils in the pathogenesis of PAH has received little attention [38], although the perivascular accumulation of macrophages

and neutrophils contributes to disease progression and has been observed in MCT-induced PAH [39]. In these two models, we measured the main indicators of PAH to determine the degree of disease progression in each case (Fig. 5). First, right ventricular systolic pressure (RVSP), the gold standard diagnostic procedure for PAH [40], was significantly elevated in both PAH models (Fig. 5A, B), although this increase was most pronounced in the SuHx group (Fig. 5B). Second, to assess pulmonary vascular remodeling, we analyzed vessels in lung histological preparations by measuring the medial wall thickness and medial wall area (Fig. 5C) from histological preparations. As shown in Fig. 5D and E, significant differences were found between the PAH groups and the control group,
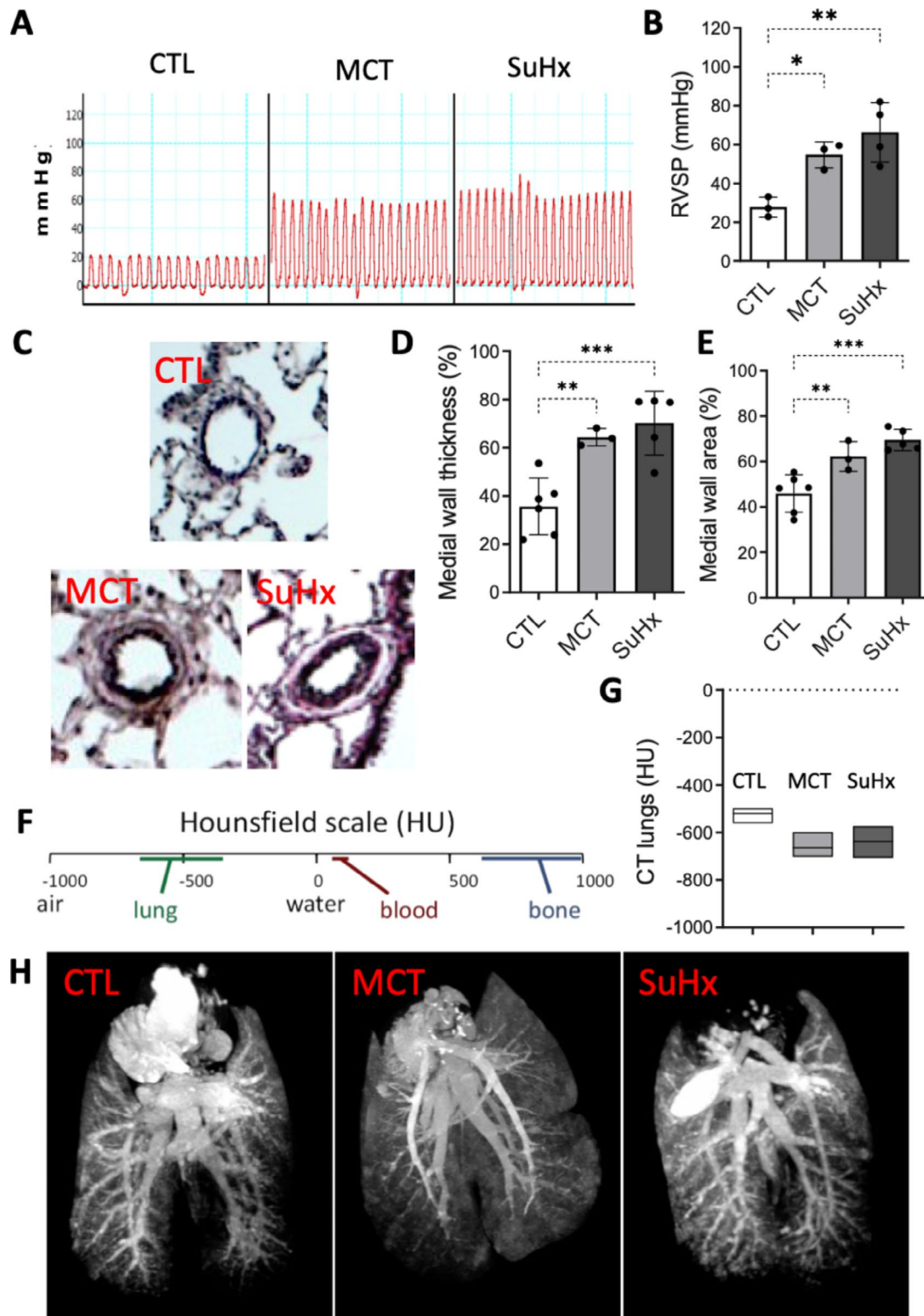
Fig. 5 **A**) Representative plots of RVSP values for each animal group. **B**) Measurement of right ventricular pressure after disease development. Values are presented as mean ± SD, **p-value < 0.01, ***p-value < 0.001 assessed by One-way ANOVA. **C**) Representative images of elastic staining of arterioles in the lung sections of each group. Measurement of vascular remodeling: **D**) medial wall thickness and (**E**) medial wall area. Values are presented as mean ± SD, **p-value < 0.01, ***p-value < 0.001 assessed by the One-way ANOVA test. **F**) Diagram of X-ray attenuation in different tissues quantified in HU. **G**) Measurement of the Hounsfield Units (HU) in three VOIs of each lung image acquired by CT. **H**) Maximum Intensity Projection (MIP) reconstruction of CT images of the pulmonary vasculature of perfused lungs, using a radiopaque casting agent

with the highest values found in the SuHx group, again suggesting more severe PAH development in the hypoxic model. Third, vascular remodeling was also confirmed at the end of the experiment by intravascular perfusion of the lungs via Microfil®, which acts as an optical or computed tomography (CT) contrast agent [41]. In our case, the resulting pulmonary vascular casting was imaged by CT imaging of the lungs, enabling complete visualization and quantification of the pulmonary vasculature using the typical scale in Hounsfield units (HU) (Fig. 5F, G). A decrease in HU indicated a microvasculature reduction in the MCT and SuHx models (Fig. 5F, G). This is visible in the different PAH models and controls shown in Fig. 5H. The moderate loss of small blood vessels in the MCT and SuHx groups (Fig. 5H) should be accompanied by typical signs of PAH, such as an increase in vasculature resistance due to changes in wall stiffness, vasoconstriction, or structural changes, and, as a consequence, to maintain cardiac output, right ventricle (RV) hypertrophy and RV failure in the latest phases.

Cardiac MRI (Figs. 6, S4) was used as the reference modality to determine LV and RV function. The MRI results revealed that the SuHx rat model exhibited a more severe LV dysfunction (Fig. 6B-D) and RV hypertrophic phenotype (Fig. 6E-I) than most MCT animals did after three weeks of disease progression. The decrease in LV ejection fraction observed in both animal models (Fig. 6B) is likely to be related to the observed RV dysfunction and the Frank-Starling mechanism associated with LV underfilling due to reduced pulmonary artery blood flow, thus maintaining a balanced output between the ventricles. The RV hypertrophy was evidenced by a more pronounced decrease in the RV ejection fraction (RV EF) (Fig. 6E), an increase in the RV end-systolic volume index (Fig. 6F), a decrease of the right ventricle end-diastolic volume index (RV SVi) (Fig. 6H) and a clear increase in the Fulton index (Fig. 6I) in this group. This finding is consistent with our previous measurements of RVSP and arterial wall thickness (Fig. 5). However, individual MCT animals presented a severe phenotype characterized by a septal flattening and a reduction in LV EDVi (Fig. 6C). High heterogeneity and marked cardiac remodeling in some MCT animals have been described previously [42], especially using similar experimental time frames. Compared with other studies, we decided to shorten the period after MCT administration (to a maximum of three weeks) for ethical reasons and to avoid the severe multiorgan toxicity of this alkaloid drug, the consequences of which are particularly critical in the following weeks, when mortality increases significantly in this model [43]. In the MCT model, despite the intersubject variability, signs of severe RV dysfunction are usually found at later exposures (more than six weeks of disease progression to induce PAH) [44]. In the trend

toward personalized medicine, monitoring the observed individual PAH phenotypes of different animal models is essential for further studies in this field, and imaging is well positioned because of the harmless characteristics of MRI. Additional imaging-based parameters of diastolic and systolic function obtained from cardiac MRI data confirmed the differences and variability of this model, as shown in Fig. 6.

After characterizing the vascular and ventricular phenotypes of the MCT and SuHx models and confirming their cardiopulmonary dysfunction, we investigated the possibility of performing neutrophil infiltration studies via targeted PET imaging with ^{68}Ga-IONP-cFLFLF. Our previous work demonstrated increased uptake of this nanoradiotracer in an acute inflammatory lung model and minimal uptake of bare ^{68}Ga-IONP in the lung [16]. We hypothesized that this nanoradiotracer could also be used to detect neutrophil recruitment in moderately injured lungs, such as the PAH models studied here, and to highlight critical differences in the role of neutrophil infiltration in PAH. Briefly, ^{68}Ga-IONP-cFLFLFs were synthesized and immediately administered intravenously. PET/CT was performed to evaluate the accumulation of the nanoradiotracer, as shown in Fig. 7. The biodistribution of these NPs, except in the lungs and heart, was similar to that observed in healthy animals (Fig. 3). ^{68}Ga-IONP-cFLFLFs were distributed in the liver, spleen, and kidneys, as confirmed by ex vivo gamma counting (Figs. 7A and S5). Our results revealed greater uptake of ^{68}Ga-IONP-cFLFLF in the MCT group (in both ventricles) than in the SuHx and control groups (Fig. 7B, and 7C). However, the wide dispersion of the data obtained for standardized uptake values (SUVs) indicates, like other imaging techniques, high heterogeneity that renders the differences between groups insignificant. Despite this cardiac heterogeneity in the MCT model, the presence of ^{68}Ga-IONP-cFLFLF was also significantly greater in the lungs of this group than in those of the SuHx group (Fig. 7D). These findings suggest that neutrophil infiltration was greater in the lungs of the MCT model than in those of the SuHx model.

The different ^{68}Ga-IONP-cFLFLF distributions in the lungs of MCT and SuHx animals may be due to the greater number of neutrophils and the inflammatory effect of MCT [45], which is known to cause pneumotoxicity [46], and acute respiratory distress [42]. Previous studies performed with invasive techniques, have shown that progressive MCT-induced PAH leads to increased lung inflammation characterized by leukocyte infiltration, neutrophil activation, and increased expression of proinflammatory cytokines [45]. In contrast, there was no evidence of ^{68}Ga-IONP-cFLFLF accumulation in the SuHx model within the time frame of our experiments, despite the more severe PAH phenotype (Figs. 5A-E and
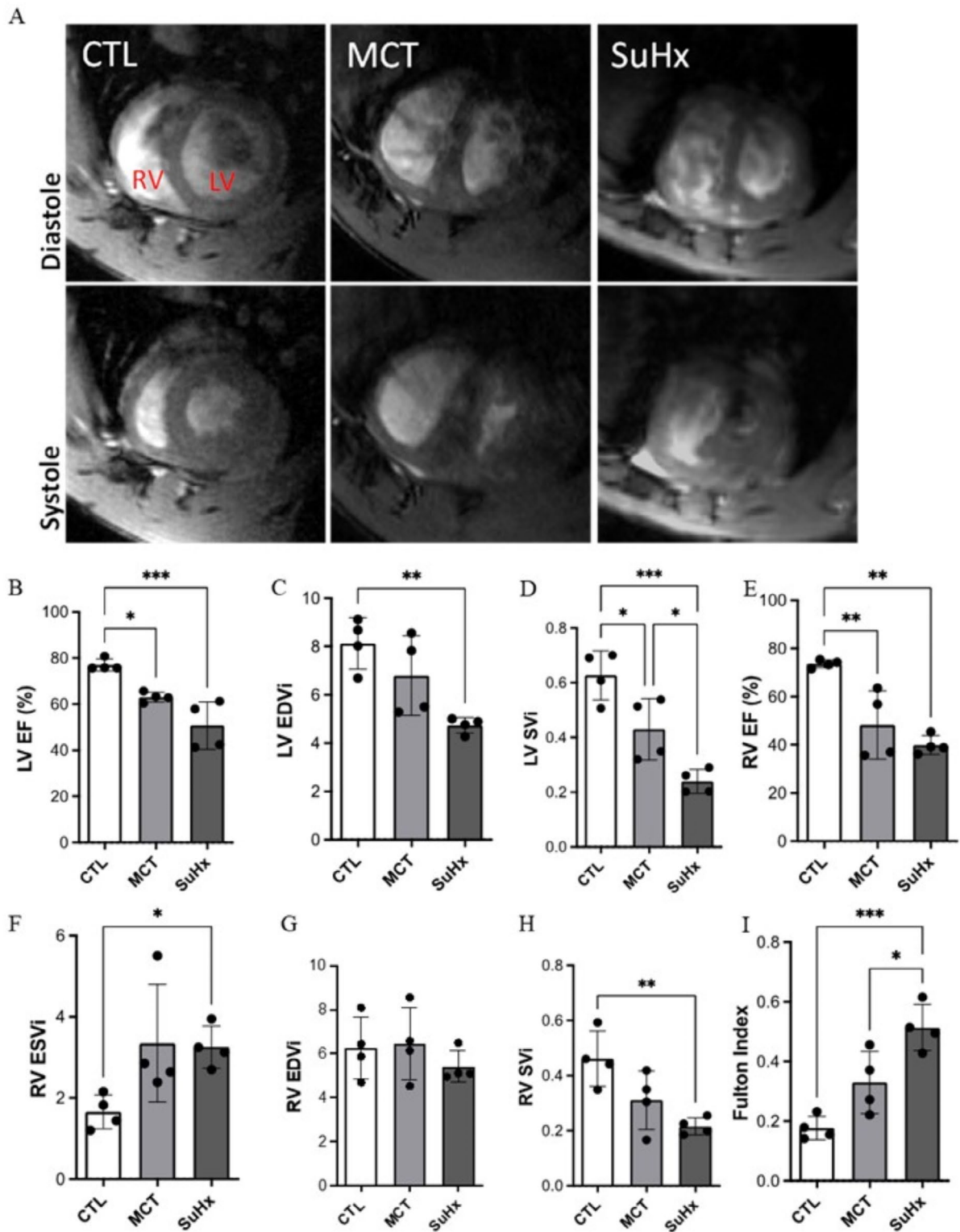
Fig. 6 MRI images and quantitative analysis of cardiac remodeling after three weeks of hypoxia or MCT exposure. **A**) Cross-sectional images of the heart of a representative animal from each group acquired by MRI showing the myocardium and epicardium of both ventricles (RV and LV) in diastole (top image) and systole (bottom image). Measurement of the left ventricle ejection fraction (LV EF, **B**), left ventricle end-diastolic volume index (LV EDVi, **C**), left ventricular stroke volume index (LV SVi, **D**), right ventricle ejection fraction (RV EF, **E**), right ventricle end-systolic volume index (RV ESVi, **F**), right ventricle end-diastolic volume index (RV EDVi, **G**), right ventricle stroke volume index (RV SVi, **H**), and Fulton index (**I**) are shown. The values are presented as mean ± SD, **$p < 0.01$, ***$p < 0.001$ and assessed via one-way ANOVA
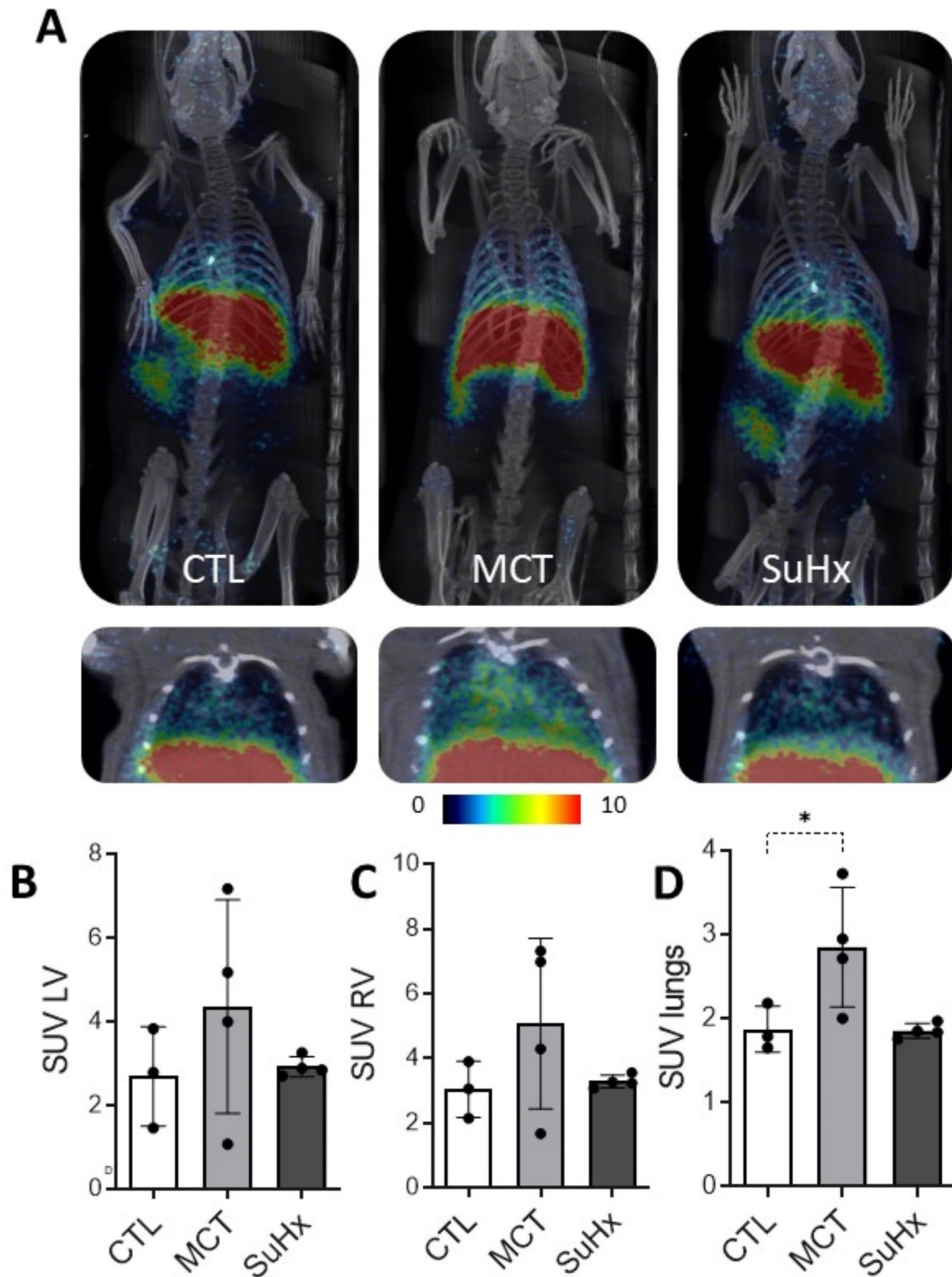
Fig. 7 Neutrophil accumulation assessed by ^{68}Ga-IONP-cFLFLF. **A**) Overlay representation of CT (maximum intensity projection, grayscale) and PET (color scale displayed over the CT images) images in the coronal plane. The bottom images correspond to the lung sections. Measurement of the standardized uptake value (SUV) in the left ventricle (SUV LV) (**B**), right ventricle (SUV RV) (**C**), and lungs (SUV lungs) (**D**). The values are expressed as the mean $\pm$ SD, * $p < 0.05$. ($n_{control}= 3$, $n_{MCT}= 4$, $n_{SuHx}= 4$)

6), likely due to the lack of neutrophil infiltration in the lungs [46].

To verify that the greater ^{68}Ga-IONP-cFLFLF uptake in the lungs of the MCT group was due to neutrophil infiltration, we performed histological analysis to correlate the presence of NPs in the lungs of PAH animals with the presence of neutrophils in the lung tissue. In clear agreement with the PET imaging data, we observed an increase in the number of inflammatory cells per area in the lung tissue sections in the MCT group, as determined by myeloperoxidase (MPO) immunostaining (Fig. 8A and Figure S6). MPO is a marker of leukocyte recruitment associated with inflammatory conditions and is produced by neutrophils, macrophages, and activated monocytes. The staining of lung sections with MPO immunostaining and subsequent image analysis (FIJI software) of different regions of interest (ROI) provided a quantification of the MPO area for the different animal groups. Figure 8B shows increased MPO staining in MCT lung sections, indicating increased leukocyte recruitment. In contrast, the values obtained for the SuHx lung sections were similar to those of the control group and lower than those of the MCT group, as observed by PET imaging (Fig. 7D). Owing to the composition of ^{68}Ga-IONP-cFLFLF, we also combined MPO staining with Perl's Prussian blue, which stains iron deposits (Fig. 8A, S7). Again, image analysis of
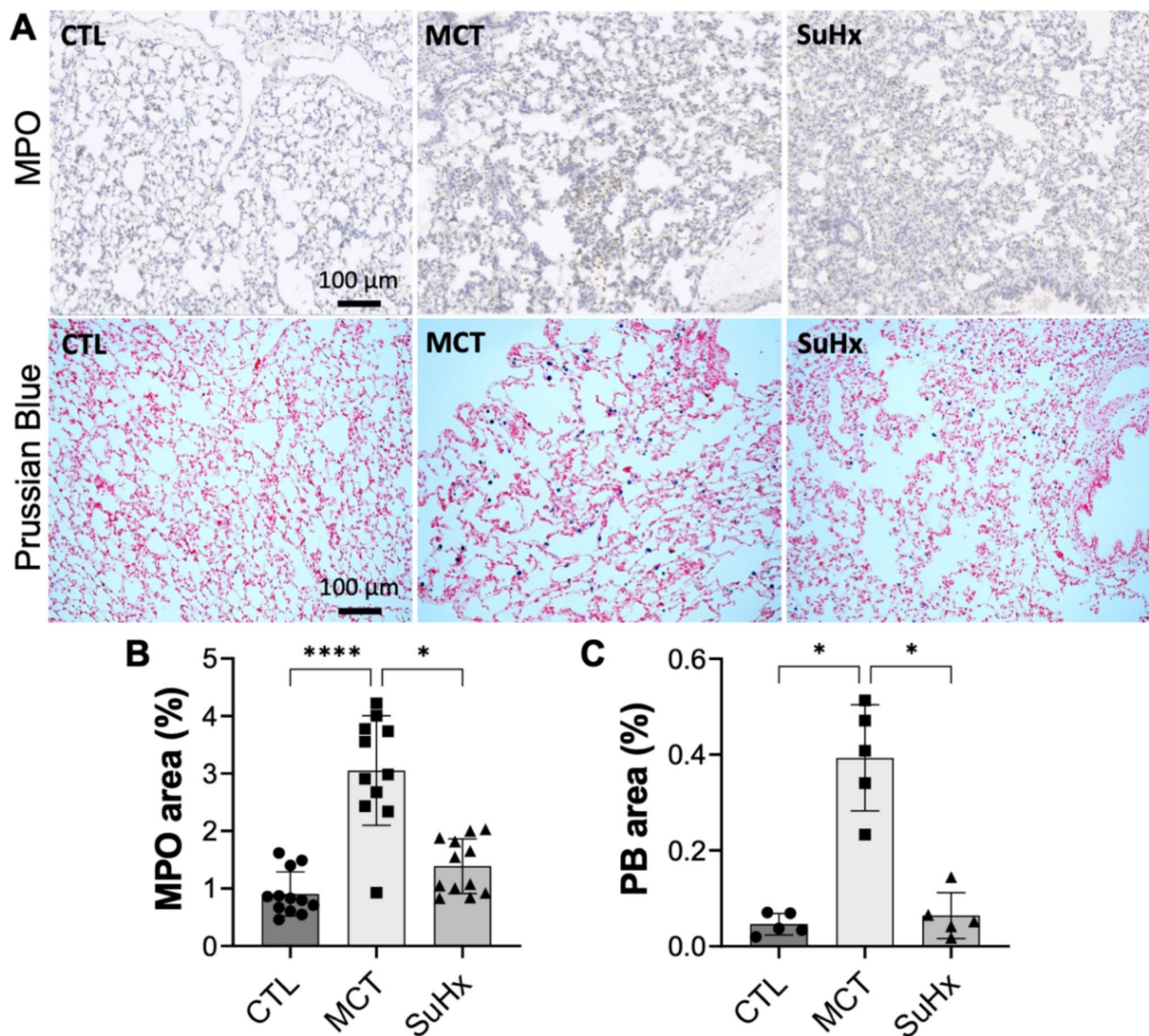

Fig. 8 Quantification of neutrophils in pulmonary tissue. **A**) Representative images of lung tissue stained with MPO (neutrophils) and Perl Prussian blue (iron). Bar graph showing the percentage of MPO (**B**) and Prussian blue (**C**) staining in different regions of interest (ROIs), such as the images shown in (**A**). The values are provided as the mean ± SD, *p-value < 0.05, ****p-value < 0.0001

regions of interest (ROIs) in different lung sections indicated a significantly greater presence of iron deposits in the MCT model, where the in vivo ^{68}Ga-IONP-cFLFLF uptake was higher. In conclusion, our results indicate that ^{68}Ga-IONP-cFLFLF is more sensitive than ^{18}F-FDG in detecting neutrophil accumulation in the MCT PAH models. Furthermore, we demonstrated that ^{68}Ga-IONP-cFLFLF constitute a valuable tool for characterizing the diverse neutrophilic-based inflammatory profiles of distinct PAH models. Future work will need to use complementary molecular biology techniques to determine the correlation between the overexpression of the FPR1 membrane receptor present in the cell membrane of neutrophils and the different stages of PAH, as well as the differences between different animal models.

Neutrophil detection with ^{18}F-FDG PET imaging

Finally, to compare the ability of ^{68}Ga-IONP-cFLFLF to detect neutrophils with the imaging gold standard used in the clinic to study sterile or septic inflammation [47, 48], PET/CT with ^{18}F-FDG radiotracer was also performed in the two different PAH models. PET/CT images of the cardiorespiratory system of some animals in the healthy, MCT, and SuHx groups are shown in Fig. 9. Interestingly, although large variability was also observed in MRI, this PET study revealed a trend (without statistical significance) for ^{18}F-FDG uptake to increase exclusively in the RV of the SuHx group compared with the healthy and MCT groups. This higher uptake in the RV, in the context of pulmonary hypertension, both in humans and animal models, has been associated with a metabolic shift of cardiomyocytes from oxidative to glycolytic metabolism rather than inflammation [49–51]. The results of ^{18}F-FDG uptake in the lung (Fig. 9D) did not coincide with those obtained with the neutrophil-targeted nanoformulation. The similar ^{18}F-FDG uptake in most healthy and PAH animals indicates that this glucose analog does not reflect the expected dynamic changes in the number of inflammatory cells or greater vascular cell proliferation or vascular remodeling (Fig. 5), at least in these animal models. Only one of the four MCT rats displays high ^{18}F-FDG uptake in contrast to previously published results of other researchers [52]. The main problem with using ^{18}F-FDG to study neutrophil infiltration in the lung is that it is not cell type specific. All cells will take it up, whether they are metabolically active or not. Therefore, this tracer is affected by many biological processes that occur in parallel with PAH, such as the reduction of microvasculature or the generation of fibrosis, which obviously affects both cell metabolism and lung cell density. In this context, more specific tools such as our nanoradiotracer based on ligand-mediated binding to the neutrophil cell membrane may be more advantageous. These interesting differences between the two PET tracers increase the

value of ^{68}Ga-IONP-cFLFLF as a specific and sensitive radiotracer for detecting neutrophil infiltration in PAH patients.

The relevance of inflammatory processes in the field of PAH has been associated with the infiltration of mixed inflammatory cells, including neutrophils, preceding structural pulmonary vascular remodeling [53]. Their involvement in angiogenesis and vascular dysfunction has also been highlighted [54, 55]. Therefore, the study of neutrophil infiltration and the development of new contrast agents such as ^{68}Ga-IONP-cFLFLF for the non-invasive detection of neutrophils in PAH is crucial for understanding the mechanisms of this disease and the development of targeted therapies. We anticipate that improved nanoparticle homogeneity and more sustainable synthetic methods will be needed to translate this technology into the clinic. However, our work demonstrates for the first time that it is possible to noninvasively detect neutrophilic infiltration in PAH models via multimodal (MRI-PET) nanoprobes. This opens up the possibility of using this method for preclinical studies of disease progression under different conditions and indicates that it is possible to generate drug nanocarriers that target neutrophils by functionalization with the FLFLF peptide.

Conclusion

This study provides promising results regarding the use of ^{68}Ga-IONP-cFLFLF as a magnetic nanoradiotracer for the targeted detection of neutrophils associated with inflammation in PAH animal models. These findings suggest that this nanoprobe can be used to investigate cell-specific inflammatory processes in PAH and the role of neutrophils in chronic inflammation. Our histological data support the direct link between neutrophil infiltration and ^{68}Ga-IONP-cFLFLF accumulation exclusively in the lungs of MCT animals in comparison with healthy and other types of PAH animal models. However, our study should be extended to determine the direct correlation between FPR1 membrane receptor expression levels and lung accumulation of ^{68}Ga-IONP-cFLFLF. The potential applications of this MRI/PET dual-mode magnetic nanoradiotracer extend beyond the specific animal models studied here. It may also have (pre)clinical relevance in other pathologies, where neutrophils play a significant role in monitoring new anti-inflammatory therapies in pulmonary hypertension. The possibility of modifying the surface of ^{68}Ga-IONP-cFLFLF with other functional molecules, such as drugs for targeted therapies, further enhances its potential utility.

Overall, this study underscores the importance of imaging in providing an individualized and longitudinal evaluation of heterogeneous and multifactorial diseases such as PAH. The use of multimodal nanoprobes, such as
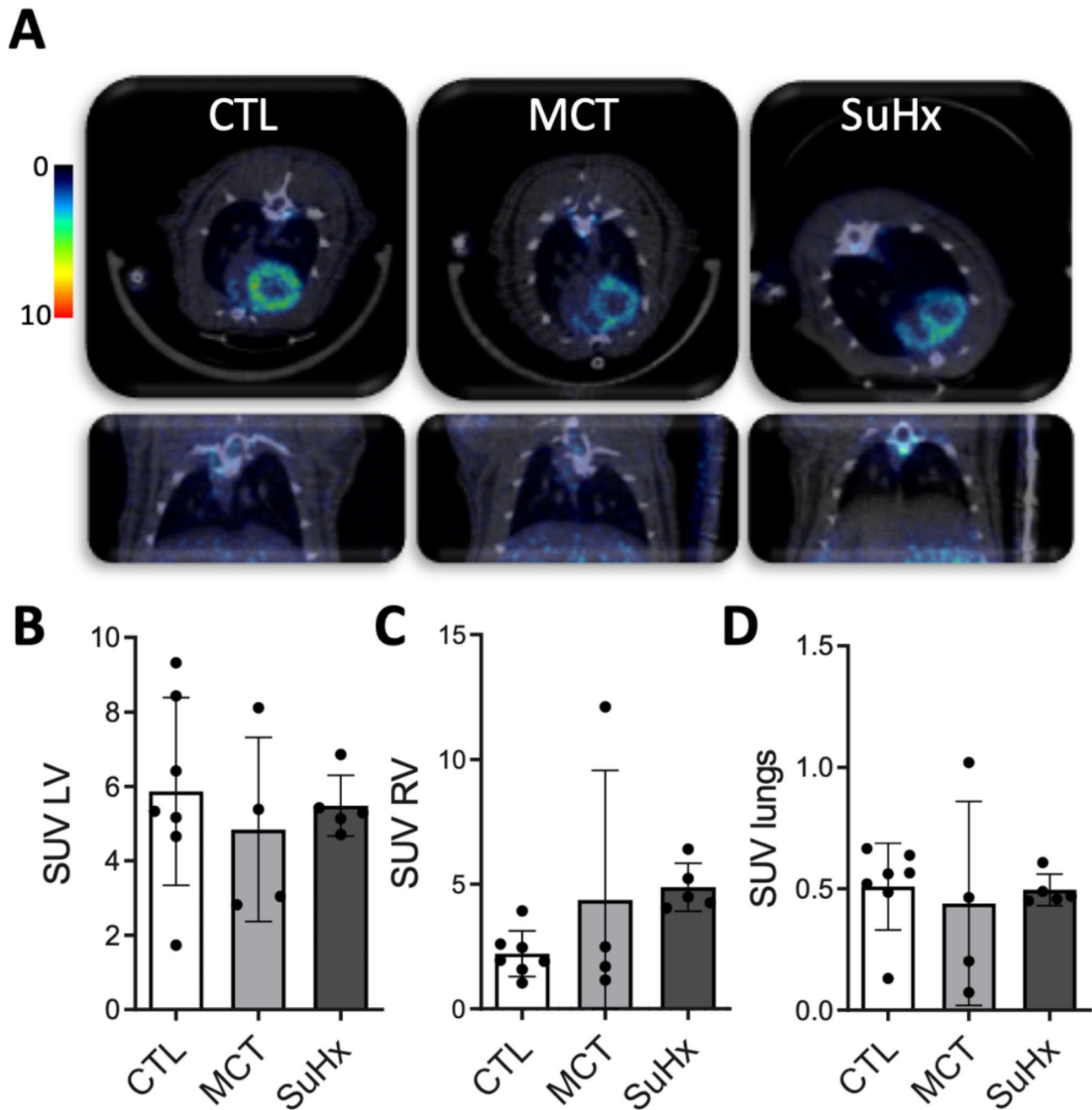
Fig. 9 Evaluation of glucose uptake by ^{18}F-FDG accumulation in organs. **A)** Overlay image of the three-dimensional reconstruction of CT (grayscale) and mid-ventricular axial PET images (color scale is represented on the left of the images). Measurement of standardized uptake values (SUVs) in the (**B**) LV, RV (**C**), and lungs (**D**). The values are presented as the mean $\pm$ SD and were assessed via one-way ANOVA. ($n_{control}$ = 6, n_{MCT} = 4, n_{SuHx} = 4)

^{68}Ga-IONP-cFLFLF, for MRI/PET imaging has the potential to facilitate the diagnosis and monitoring of diseases, as well as the development of novel therapies.

Supplementary Information

The online version contains supplementary material available at https://doi.org/10.1186/s12951-024-03000-7.

Supplementary Material 1

and Trade (Elkartek) and MICINN (PID2019-108112RB-I00 (FEDER/EU); Severo Ochoa Excellence Accreditation MCIN/AEI/10.13039/501100011033 for grant CEX2021-001136-S). CIBERES and CIBERONC were co-funded with FEDER funds and by ISCIII.

Author contributions
L.F. worked on the development of the PAH animal models and their functional characterization and wrote part of the paper. C.M.A. performed the MRI contrast agent characterization and biodistribution studies, analyzed the data, and revised the paper. M.B.C. assisted in animal experiments and tissue processing. A.B.M.C. synthesized the magnetic nanoradiotracers. D.D.S. performed and analyzed the XPS experiments. A.U.A. performed the cytotoxicity experiments and histological images. M.J.S.G. and I.A.Z. performed and analyzed the cardiac MRI experiments. L.F.M. and L.M.P. characterized the nanoparticles. E.I. supported the PET experiments. E.B. provided conceptual input and supervised experiments. S.C.R. and J.R.C. designed the experiments, supervised the research, and wrote the paper.

Data availability
No datasets were generated or analysed during the current study.

Declarations

Ethics approval and consent to participate
Animal handling was conducted under the European Council Directive 2010/63/UE. The Ethical Committee at CIC biomaGUNE and local authorities Diputación Foral de Guipuzcoa (project authorization numbers: PRO-AE-SS-225 and PRO-AE-SS-112) approved all the animal experiments.

Consent for publication
We acknowledge that the manuscript text and any associated images submitted for publication in the journal will be made freely accessible on the internet, available for view by the general public.

Competing interests
The authors declare no competing interests.

Author details
[1]Department of Diagnostic Radiology and Nuclear Medicine, University of Maryland School of Medicine, Baltimore 21201, USA
[2]Center for Cooperative Research in Biomaterials (CIC biomaGUNE), Basque Research and Technology Alliance (BRTA), Donostia 20014, Spain
[3]Euskal Herriko Unibertsitatea (UPV/EHU), Donostia 20018, Spain
[4]Centro de investigación en red de enfermedades respiratorias (CIBERES), Instituto de Salud Carlos III, Madrid 28029, Spain
[5]Center for Cooperative Research in Bioscience (CIC bioGUNE), Basque Research and Technology Alliance (BRTA), Derio 4810, Spain
[6]Centro de investigación en red cáncer (CIBERONC), Instituto de Salud Carlos III, Madrid 28029, Spain
[7]Ikerbasque, Basque Foundation for Science Ikerbasque, Bilbao 48013, Spain
[8]Departamento de Química en Ciencias Farmacéuticas, Universidad Complutense de Madrid, Madrid 28040, Spain

References
1. Groth A, Vrugt B, Brock M, Speich R, Ulrich S, Huber LC. Inflammatory cytokines in pulmonary hypertension. Respir Res. 2014;15:47.
2. Wang R-r, Yuan T-y, Wang J-m, Chen Y-c, Zhao J-l, Li M-t. Fang L-h, Du G-h: immunity and inflammation in pulmonary arterial hypertension: from pathophysiology mechanisms to treatment perspective. Pharmacol Res. 2022;180:106238.
3. Ferrian S, Cao A, McCaffrey EF, Saito T, Greenwald NF, Nicolls MR, Bruce T, Zamanian RT, Rosario PD, Rabinovitch M, Angelo M. Single-cell imaging maps inflammatory cell subsets to pulmonary arterial hypertension vasculopathy. Am J Respir Crit Care Med. 2024;209:206–18.
4. Sweatt AJ, Miyagawa K, Rhodes CJ, Taylor S, Del Rosario PA, Hsi A, Haddad F, Spiekerkoetter E, Bental-Roof M, Bland RD, et al. Severe pulmonary arterial hypertension is characterized by increased neutrophil elastase and relative elafin deficiency. Chest. 2021;160:1442–58.
5. Vass L, Fisk M, Cheriyan J, Mohan D, Forman J, Oseni A, Devaraj A, Mäki-Petäjä KM, McEniery CM, Fuld J et al. Quantitative (18)F-fluorodeoxyglucose positron emission tomography/computed tomography to assess pulmonary inflammation in COPD. ERJ Open Res 2021, 7.
6. Marsboom G, Wietholt C, Haney CR, Toth PT, Ryan JJ, Morrow E, Thenappan T, Bache-Wiig P, Piao L, Paul J, et al. Lung ^{18}F-fluorodeoxyglucose positron emission tomography for diagnosis and monitoring of pulmonary arterial hypertension. Am J Respir Crit Care Med. 2012;185:670–9.
7. Maier A, Liao SL, Lescure T, Robson PM, Hirata N, Sartori S, Narula N, Vergani V, Soultanidis G, Morgenthau A, et al. Pulmonary artery 18F-fluorodeoxyglucose uptake by PET/CMR as a marker of pulmonary hypertension in sarcoidosis. JACC: Cardiovasc Imaging. 2022;15:108–20.
8. Park J-B, Suh M, Park JY, Park JK, Kim Y-i, Kim H, Cho YS, Kang H, Kim K, Choi J-H, et al. Assessment of inflammation in pulmonary artery hypertension by 68Ga-mannosylated human serum albumin. Am J Respir Crit Care Med. 2020;201:95–106.
9. Hoshyar N, Gray S, Han H, Bao G. The effect of nanoparticle size on in vivo pharmacokinetics and cellular interaction. Nanomedicine. 2016;11:673–92.
10. Locke LW, Chordia MD, Zhang Y, Kundu B, Kennedy D, Landseadel J, Xiao L, Fairchild KD, Berr SS, Linden J, Pan D. A novel neutrophil-specific PET imaging agent: cFLFLFK-PEG-^{64}Cu. J Nucl Med. 2009;50:790–7.
11. Dorward DA, Lucas CD, Chapman GB, Haslett C, Dhaliwal K, Rossi AG. The role of formylated peptides and formyl peptide receptor 1 in governing neutrophil function during acute inflammation. Am J Pathol. 2015;185:1172–84.
12. Chen J, Cheng H, Dong Q, Chen F, Huang Z, Zhang Y, Pan D, Xiong W. [99mTc] cFLFLF for early diagnosis and therapeutic evaluation in a rat model of acute osteomyelitis. Mol Imaging Biology. 2015;17:337–44.
13. Charles EJ, Chordia MD, Zhao Y, Zhang Y, Mehaffey JH, Glover DK, Dimastromatteo J, Chancellor WZ, Sharma AK, Kron IL, et al. SPECT imaging of lung ischemia-reperfusion injury using [99mTc]cFLFLF for molecular targeting of formyl peptide receptor 1. Am J Physiology-Lung Cell Mol Physiol. 2020;318:L304–13.
14. Mattila JT, Beaino W, White AG, Nyiranshuti L, Maiello P, Tomko J, Frye LJ, Fillmore D, Scanga CA, Lin PL, et al. Retention of (64)Cu-FLFLF, a formyl peptide receptor 1-specific PET probe, correlates with macrophage and neutrophil abundance in lung granulomas from cynomolgus macaques. ACS Infect Dis. 2021;7:2264–76.
15. Loitto VM, Rasmusson B, Magnusson KE. Assessment of neutrophil N-formyl peptide receptors by using antibodies and fluorescent peptides. J Leukoc Biol. 2001;69:762–71.
16. Pellico J, Lechuga-Vieco AV, Almarza E, Hidalgo A, Mesa-Nuñez C, Fernández-Barahona I, Quintana JA, Bueren J, Enríquez JA, Ruiz-Cabello J, Herranz F. In vivo imaging of lung inflammation with neutrophil-specific 68Ga nanoradiotracer. Sci Rep. 2017;7:13242.
17. Sandström T, Bjermer L, Rylander R. Lipopolysaccharide (LPS) inhalation in healthy subjects increases neutrophils, lymphocytes and fibronectin levels in bronchoalveolar lavage fluid. Eur Respir J. 1992;5:992–6.
18. Pellico J, Ruiz-Cabello J, Saiz-Alía M, Del Rosario G, Caja S, Montoya M, Fernández de Manuel L, Morales MP, Gutiérrez L, Galiana B, et al. Fast synthesis and bioconjugation of (68) Ga core-doped extremely small iron oxide nanoparticles for PET/MR imaging. Contrast Media Mol Imaging. 2016;11:203–10.
19. Fernández-Barahona I, Muñoz-Hernando M, Herranz F. Microwave-driven synthesis of iron-oxide nanoparticles for molecular imaging. Molecules. 2019;24:1224.
20. Williams MJ, Sánchez E, Aluri ER, Douglas FJ, MacLaren DA, Collins OM, Cussen EJ, Budge JD, Sanders LC, Michaelis M, et al. Microwave-assisted synthesis of highly crystalline, multifunctional iron oxide nanocomposites for imaging applications. RSC Adv. 2016;6:83520–8.
21. Carregal-Romero S, Miguel-Coello AB, Martínez-Parra L, Martí-Mateo Y, Hernansanz-Agustín P, Fernández-Afonso Y, Plaza-García S, Gutiérrez L, Muñoz-Hernández MdM, Carrillo-, Romero J et al. Ultrasmall manganese ferrites for in vivo catalase mimicking activity and multimodal bioimaging. *Small* 2022, 18:2106570.
22. Groult H, Carregal-Romero S, Castejón D, Azkargorta M, Miguel-Coello A-B, Pulagam KR, Gómez-Vallejo V, Cousin R, Muñoz-Caffarel M, Lawrie CH, et al. Heparin length in the coating of extremely small iron oxide nanoparticles regulates in vivo theranostic applications. Nanoscale. 2021;13:842–61.

23. Pellico J, Fernández-Barahona I, Ruiz-Cabello J, Gutiérrez L, Muñoz-Hernando M, Sánchez-Guisado MJ, Aiestaran-Zelaia I, Martínez-Parra L, Rodríguez I, Benzton J, Herranz F. HAP-Multitag, a PET and positive MRI contrast Nanotracer for the Longitudinal characterization of vascular calcifications in atherosclerosis. ACS Appl Mater Interfaces. 2021;13:45279–90.

24. Xu Y, Wu H, Huang J, Qian W, Martinson DE, Ji B, Li Y, Wang YA, Yang L, Mao H. Probing and enhancing ligand-mediated active targeting of tumors using Sub-5 nm Ultrafine Iron Oxide nanoparticles. Theranostics. 2020;10:2479–94.

25. Silva-Silva MJ, Mijangos-Ricardez OF, Vázquez-Hipólito V, Martinez-Vargas S, López-Luna J. Single and mixed adsorption of cd(II) and cr(VI) onto citrate-coated magnetite nanoparticles. Desalination Water Treat. 2016;57:4008–17.

26. Saito K, Xu T, Ishikita H. Correlation between CO stretching vibrational frequency and pK(a) shift of carboxylic acids. J Phys Chem B. 2022;126:4999–5006.

27. Zheng X, Xu K, Wang Y, Shen R, Wang Q. Study of hydrogen explosion control measures by using l-phenylalanine for aluminum wet dust removal systems. RSC Adv. 2018;8:41308–16.

28. Ta HT, Li Z, Wu Y, Cowin G, Zhang S, Yago A, Whittaker AK, Xu ZP. Effects of magnetic field strength and particle aggregation on relaxivity of ultra-small dual contrast iron oxide nanoparticles. Mater Res Express. 2017;4:116105.

29. Yang M, Christoforidis GA, Figueredo T, Heverhagen JT, Abduljalil A, Knopp MV. Dosage determination of ultrasmall particles of iron oxide for the delineation of microvasculature in the Wistar rat brain. Invest Radiol. 2005;40:655–60.

30. Wáng YXJ, Idée J-M. A comprehensive literatures update of clinical researches of superparamagnetic resonance iron oxide nanoparticles for magnetic resonance imaging. Quant Imaging Med Surg. 2017;7:88–122.

31. Li Y, Du Y, Zhou Y, Chen Q, Luo Z, Ren Y, Chen X, Chen G. Iron and copper: critical executioners of ferroptosis, cuproptosis and other forms of cell death. Cell Communication Signal. 2023;21:327.

32. Kolosnjaj-Tabi J, Lartigue L, Javed Y, Luciani N, Pellegrino T, Wilhelm C, Alloyeau D, Gazeau F. Biotransformations of magnetic nanoparticles in the body. Nano Today. 2016;11:280–4.

33. Pellico J, Vass L, Carrascal-Miniño A, Man F, Kim J, Sunassee K, Parker D, Blower PJ, Marsden PK, de Rosales TM. R: In vivo real-time positron emission particle tracking (PEPT) and single particle PET. Nat Nanotechnol 2024.

34. Ryan JJ, Marsboom G, Archer SL. Rodent models of group 1 pulmonary hypertension. Handb Exp Pharmacol. 2013;218:105–49.

35. Vitali SH, Hansmann G, Rose C, Fernandez-Gonzalez A, Scheid A, Mitsialis SA, Kourembanas S. The Sugen 5416/hypoxia mouse model of pulmonary hypertension revisited: long-term follow-up. Pulm Circ. 2014;4:619–29.

36. Taraseviciene-Stewart L, Kasahara Y, Alger L, Hirth P, Mc Mahon G, Waltenberger J, Voelkel NF, Tuder RM. Inhibition of the VEGF receptor 2 combined with chronic hypoxia causes cell death-dependent pulmonary endothelial cell proliferation and severe pulmonary hypertension. Faseb j. 2001;15:427–38.

37. Bueno-Beti C, Sassi Y, Hajjar RJ, Hadri L. Pulmonary Artery Hypertension Model in Rats by Monocrotaline Administration. In Experimental Models of Cardiovascular Diseases: Methods and Protocols. Edited by Ishikawa K. New York, NY: Springer New York; 2018: 233–241.

38. Taylor S, Dirir O, Zamanian RT, Rabinovitch M, Thompson AAR. The role of neutrophils and neutrophil elastase in pulmonary arterial hypertension. Front Med (Lausanne). 2018;5:217.

39. Schultze AE, Wagner JG, White SM, Roth RA. Early indications of monocrotaline pyrrole-induced lung injury in rats. Toxicol Appl Pharmcol. 1991;109:41–50.

40. Kawaguchi T, Kitamura H, Kato S, Ohtoshi R, Tabata E, Oda T, Hagiwara E, Fukui K, Yatera K, Ogura T. Right ventricular systolic pressure as a prognostic factor for pulmonary hypertension with interstitial lung disease. Eur Respir J. 2019;54:PA1304.

41. Deng Y, Rowe KJ, Chaudhary KR, Yang A, Mei SHJ, Stewart DJ. Optimizing imaging of the rat pulmonary microvasculature by micro-computed tomography. Pulm Circ. 2019;9:2045894019883613.

42. Hołda MK, Szczepanek E, Bielawska J, Palka N, Wojtysiak D, Frączek P, Nowakowski M, Sowińska N, Arent Z, Podolec P, Kopeć G. Changes in heart morphometric parameters over the course of a monocrotaline-induced pulmonary arterial hypertension rat model. J Translational Med. 2020;18:262.

43. Vélez-Rendón D, Zhang X, Gerringer J, Valdez-Jasso D. Compensated right ventricular function of the onset of pulmonary hypertension in a rat model depends on chamber remodeling and contractile augmentation. Pulm Circ. 2018;8:2045894018800439.

44. Singal PK, Farahmand F, Hill MF. Antioxidant and oxidative stress changes in experimental cor pulmonale. Mol Cell Biochem. 2004;260:21–9.

45. Ahmed LA, Obaid AA, Zaki HF, Agha AM. Role of oxidative stress, inflammation, nitric oxide and transforming growth factor-beta in the protective effect of diosgenin in monocrotaline-induced pulmonary hypertension in rats. Eur J Pharmacol. 2014;740:379–87.

46. Hilliker KS, Bell TG, Roth RA. Pneumotoxicity and thrombocytopenia after single injection of monocrotaline. Am J Physiol Heart Circ Physiol. 1982;242:H573–9.

47. de Prost N, Tucci MR, Melo MF. Assessment of lung inflammation with 18F-FDG PET during acute lung injury. AJR Am J Roentgenol. 2010;195:292–300.

48. Casali M, Lauri C, Altini C, Bertagna F, Cassarino G, Cistaro A, Erba AP, Ferrari C, Mainolfi CG, Palucci A, et al. State of the art of (18)F-FDG PET/CT application in inflammation and infection: a guide for image acquisition and interpretation. Clin Transl Imaging. 2021;9:299–339.

49. Ahmadi A, Ohira H, Mielniczuk LM. FDG PET imaging for identifying pulmonary hypertension and right heart failure. Curr Cardiol Rep. 2014;17:555.

50. Graham BB, Kumar R, Mickael C, Sanders L, Gebreab L, Huber KM, Perez M, Smith-Jones P, Serkova NJ, Tuder RM. Severe pulmonary hypertension is associated with altered right ventricle metabolic substrate uptake. Am J Physiol Lung Cell Mol Physiol. 2015;309:L435–440.

51. Hagan G, Southwood M, Treacy C, Ross RM, Soon E, Coulson J, Sheares K, Screaton N, Pepke-Zaba J, Morrell NW, Rudd JH. (18)FDG PET imaging can quantify increased cellular metabolism in pulmonary arterial hypertension: a proof-of-principle study. Pulm Circ. 2011;1:448–55.

52. Marsboom G, Wietholt C, Haney CR, Toth PT, Ryan JJ, Morrow E, Thenappan T, Bache-Wiig P, Piao L, Paul J, et al. Lung 18F-fluorodeoxyglucose positron emission tomography for diagnosis and monitoring of pulmonary arterial hypertension. Am J Respir Crit Care Med. 2012;185:670–9.

53. Humbert M, Guignabert C, Bonnet S, Dorfmüller P, Klinger JR, Nicolls MR, Olschewski Andrea J, Pullamsetti SS, Schermuly RT, Stenmark Kurt R, Rabinovitch M. Pathology and pathobiology of pulmonary hypertension: state of the art and research perspectives. Eur Respir J. 2019;53:1801887.

54. Sun H, Du Z, Zhang X, Gao S, Ji Z, Luo G, Pan S. Neutrophil extracellular traps promote proliferation of pulmonary smooth muscle cells mediated by CCDC25 in pulmonary arterial hypertension. Respir Res. 2024;25:183.

55. Aldabbous L, Abdul-Salam V, McKinnon T, Duluc L, Pepke-Zaba J, Southwood M, Ainscough AJ, Hadinnapola C, Wilkins MR, Toshner M, Wojciak-Stothard B. Neutrophil extracellular traps promote angiogenesis: evidence from vascular pathology in pulmonary hypertension. Arterioscler Thromb Vasc Biol. 2016;36:2078–87.

Publisher's note